ISAR Imaging of a Windmill
– Measurement and Simulation

Chenchen Li[1], Shang-Te Yang[2], and Hao Ling[3]

Dept. of Electrical and Computer Engineering, The University of Texas at Austin, Austin, USA

[1]cjli@utexas.edu, [2]shangte.yang@utexas.edu, [3]ling@ece.utexas.edu

Abstract—**Inverse synthetic aperture radar (ISAR) images of a windmill are presented. In-situ measurement data of an 18-blade windmill are collected using an ultra-wideband radar. The measured signatures are compared to simulation results based on physical optics. The backscattering phenomenology is examined in the sinogram, spectrogram, and ISAR image domains. In addition, a composite image is generated from multiple ISAR snapshots to reveal the entire windmill structure.**

Index Terms—**Wind farm, radar, radar imaging.**

I. INTRODUCTION

The interaction between wind farms and radar waves is a topic of current interest [1]-[4]. The time-varying radar scattering from rotating blades of a wind turbine creates Doppler clutter that may interfere with radar detection and tracking. Understanding the detailed radar scattering phenomenology of wind turbines is therefore an important step toward assessment and mitigation. Significant efforts have been devoted in the electromagnetics community to simulating, measuring, and analyzing the radar signatures of wind turbines [5]-[10].

Inverse synthetic aperture radar (ISAR) imaging is an established technique to acquire the detailed scattering features of a complex target. The standard ISAR scenario entails a target under constant rotational motion, which is typically created in the laboratory by rotating the target on a turntable. Since turbine blades undergo relatively steady rotation, it should be possible to generate an ISAR image of a turbine from its time-varying radar signatures observed from a stationary radar without any additionally imposed motion. The resulting ISAR image may provide useful information on the scattering mechanisms and the motion anomalies associated with the turbine.

In this paper, we present measured and simulated ISAR images of a small 18-blade windmill. The measurement results are acquired using a portable ultra-wideband radar system (PulsON 410) from Time Domain Corporation [11]. The measured signatures are compared to simulation results computed using the physical optics (PO) method in the commercial software FEKO [12]. Image formation details are discussed and the resulting scattering phenomenology is examined.

II. METHODOLOGY

A. Measurement Synopsis

In-situ measurements were made at a local windmill in Cedar Park, Texas using the Time Domain ultra-wideband radar system. Two dual-ridged broadband horns were used as transmitting and receiving antennas. The radar emits short pulses at a pulse repetition frequency of 10 MHz with an equivalent frequency bandwidth from 3.1 to 5.3 GHz. The transmitted pulses are pseudo-random coded to overcome the 15 m maximum unambiguous range and improve the signal-to-noise ratio. The radar sampling rate for consecutive range profiles was set to 200 Hz. This sampling rate is upper-bounded by a number of factors including the number of range bins, the number of coherently integrated pulses to form a range profile, as well as the radar-to-computer data transfer rate. It must be greater than the maximum Doppler extent of the windmill return to coherently process the range profiles into an unaliased ISAR image.

The measurement distance was approximately 25 m to the hub of the windmill. The windmill from the radar perspective was approximately at a $\theta = 45°$ elevation angle onto the frontal, head-on view of the windmill. Fig. 1(a) shows the target windmill from the perspective of the radar and Fig. 1(b) shows the measurement collection setup including the two horn antennas, the PulsON 410 radar unit (of size 12 cm x 9 cm x 3.5 cm), and a laptop computer.

(a)   (b)

Fig. 1. (a) Windmill photo from the radar perspective. (b) Collection setup including two dual-ridged broadband horn antennas, the Time Domain PulsON 410 radar unit, and a laptop computer.

The approximate diameter of the windmill rotor is 5 m with 18 1.6 m-long blades. The rotation rate was approximately 15 rpm during the collection. By taking the frontal perspective (at a +45° elevation angle), we can reduce the maximum down-range and Doppler extent of the windmill. The maximum down-range extent is estimated to be 5 sin45° m = 3.5 m and the maximum Doppler extent can be estimated from:

$$f_{D,max} = 2\left(\frac{2R\Omega}{\lambda}\right)\sin\theta \qquad (1)$$

where R is the radius of the rotor, Ω is the rotation rate, λ is the wavelength, θ is the elevation angle from the radar perspective, and the extra factor of two accounts for the both the positive and negative Doppler returns from the blades. Thus, $f_{D,max}$ at 4.3 GHz is 159 Hz and our chosen 200 Hz sampling is sufficient to capture the variation from consecutive range profiles.

B. Simulation Synopsis

A FEKO model of the windmill was created using the approximate dimensions and a 20° pitch of the blades. For simplicity, only the blades of the windmill were included in the simulation. The blades were assumed to be perfectly conducting. Fig. 2(a) shows a diagram of the measurement layout and Fig. 2(b) shows the FEKO model.
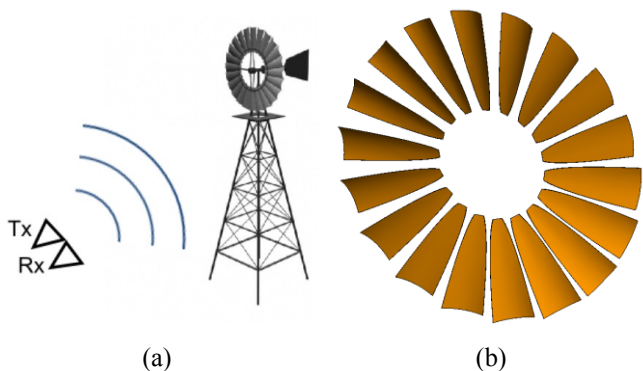

Fig. 2. (a) Measurement layout. (b) FEKO model.

The physical optics plus full ray tracing (i.e. PO with shadowing) solver in FEKO was used in the simulation. Far-field conditions were assumed on both transmit and receive in the simulation. The frequency range was the same as the measurement using 75 frequency points to provide a sufficient down-range window without aliasing. To simulate the rotating turbine blades, we rotated the blade geometry to form consecutive CAD files and carried out FEKO simulation for each file from the approximate measurement incident angle. The result of the simulation is the radar signature as a function of time. The required angular sampling between snapshots can be estimated as $\Delta\phi = \Omega/f_{D,max}$. Thus, to match the 200 Hz Doppler extent used in the measurement, the angular sampling should be spaced by 0.45° or less. This number was rounded down to 0.4° in simulation.

III. MEASUREMENT AND SIMULATION RESULTS

The dynamic signatures from the measured and simulated backscattered data versus time (or blade rotation angle) are post-processed into sinograms, spectrograms, and ISAR images. Data for the vertical-polarization-on-transmit, vertical-polarization-on-receive case are shown. The measured data are not calibrated in terms of absolute radar cross section level. Additionally, the measurement data have been motion filtered during the data collection to remove stationary clutter.

A. Sinogram

The measured and simulated sinograms (i.e., range profiles versus time) are shown in Fig. 3. The range profile in the simulation is obtained by inverse Fourier transforming the frequency response. There is reasonable agreement between measurement and simulation. The strong periodic return near zero down-range is the flash of a single blade as it becomes perpendicular to the radar line-of-sight (RLOS). There are also 18 faint tracks that extend beyond the blade flash. Each track corresponds to the return from the outer tip of one of the 18 blades. It follows the expected sinusoidal trajectory through the first half of a rotation. Due to the pitch of the blade, the trajectory of the second half of the rotation is much weaker in strength and becomes difficult to see within the 40 dB dynamic range. There should also be faint tracks that correspond to returns from the inner blade tips. However, they are much
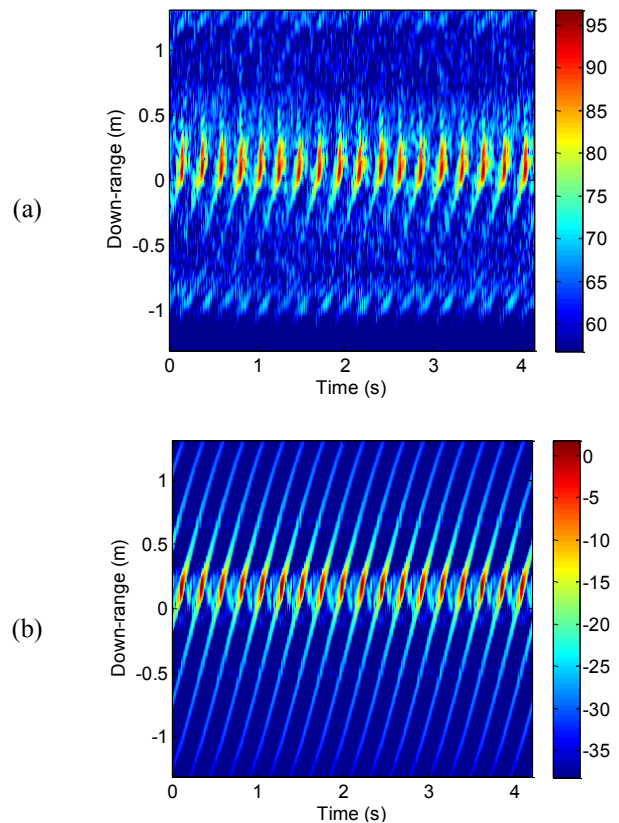

Fig. 3. Sinogram. (a) Measurement. (b) Simulation.

weaker and are again difficult to see within a 40 dB dynamic range.

Note that we were not able to fully capture the down-range extent of the windmill in measurement due to the need for a narrow range gate (set at 2.63 m) in order to achieve the 200 Hz range profile sampling rate. We have cropped the simulation plot in down-range for a one-to-one comparison with the measurement.

B. Spectrogram

By Fourier transforming the measured range profiles from the Time Domain radar, we obtain the corresponding complex frequency response. Now the time-varying Doppler behavior of the target can be examined at a single frequency. Using a short-time Fourier Transform (STFT) along the time axis, we obtain the Doppler frequency versus time plot (or the Doppler spectrogram) at 4.3 GHz. Fig. 4 shows the spectrograms obtained using the STFT with a 230 ms Hamming window. Both spectrograms show a sequence of prominent negative Doppler flashes, which occur at time instances when the blades become perpendicular to the RLOS while receding away from the radar. By comparison, the positive Doppler returns are much weaker. This confirms the observation made based on the sinograms that each blade is only prominent for half a rotation due to the blade pitch angle. The slight decrease in the maximum Doppler extent as a function of time in the measurement is due to the windmill slowing down slightly over the 4-second span.
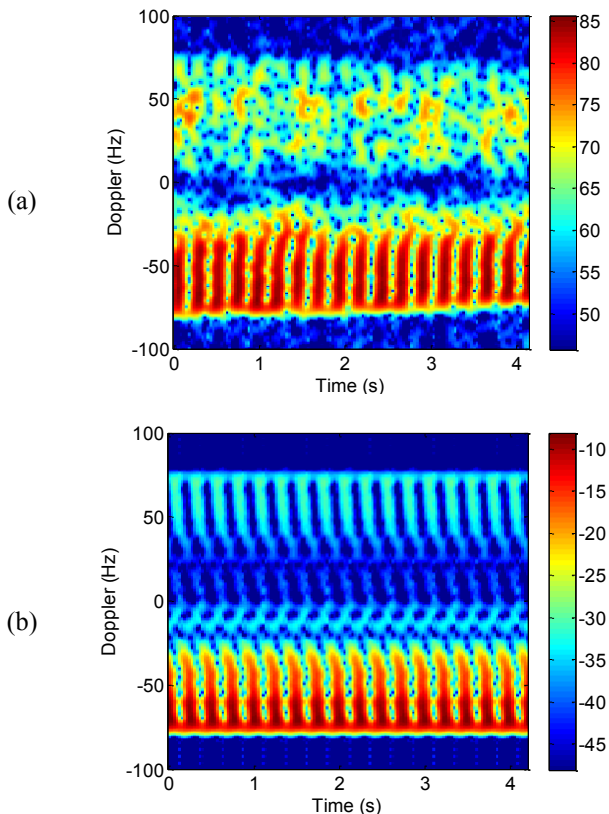

Fig. 4. Spectrogram. (a) Measurement. (b) Simulation.

C. ISAR Image

By processing the frequency response versus time data using a 2-D inverse Fourier transform, we can generate a 2-D ISAR image of the windmill [13]. If we assume a known constant rotation rate, the ISAR image can be displayed as a down-range vs. cross-range plot. This is illustrated in the following formulation:

$$Image(r, cr) = \frac{1}{k_x k_y} \iint E^s(f, \phi)\, e^{jk_x r} e^{jk_y cr}\, dk_x dk_y \quad (2)$$

$$where \begin{cases} k_x = \dfrac{4\pi f}{c} \cos\phi & \cong \dfrac{4\pi f}{c} \\[2mm] k_y = \dfrac{4\pi f}{c} \sin\phi & \cong \dfrac{4\pi f_c}{c} \phi \end{cases} \quad (3)$$

where r is the down-range, cr is the cross-range, f is the frequency, ϕ is the rotation angle, E^s is the backscattered field as a function of frequency and angle, and c is the speed of light. By making a small-angle, narrow-band approximation shown in the second part of eq. (3), where f_c is the center frequency, spectral variables k_x and k_y become decoupled and the ISAR image can be simply obtained via a 2-D inverse fast Fourier transform (IFFT) of the backscattered field sampled uniformly in frequency and angle. For measurement, the angle is related to collection time through $\phi = \Omega t$.

We use an angular swath of 20° to generate ISAR snapshots of the windmill in both simulation and measurement. As we slide the 20° angular swath along the angular (or time) axis, we can see each blade 'light up' as they become perpendicular to the RLOS near zero down-range. This is easily seen in a movie made of many consecutive ISAR frames. Here, we have shown several snapshots that highlight the sequence before, during, and after the blade flash in Fig. 5. The measurement data are presented on the left and the simulated data on the right. The snapshots going down each column are five equally spaced instances spanning 20° (4° spacing between each snapshot). The maximum blade flash occurs at the middle of the sequence, as shown by Figs. 5(c)(h). There are some minor differences between the measurement and simulation. They can be explained by the simplified geometry of the model and the physical optics simulation that ignores higher order interactions.

Focusing on the blade flash in Figs. 5(c)(h), we observe two distinct features at zero down-range. Each is a blade flash, with the one on the left much stronger than the one on the right due to the pitch of the blades. At the same time, a faint outline of the outer and inner tips of the other blades can be clearly seen in the simulation. It is less apparent in the measurement results. On the other hand, an outline of a middle ring can be noticed in the measurement data. This middle ring can be seen in the Fig. 1(a) photo, but was not included in the simulation model. Finally, due to the limited range gate, the entire turbine

was not fully captured in measurement. As a result, the image intensity beyond the ±1.32 m down-range extent is zero. This truncation effect can be noticed in the measurement data.
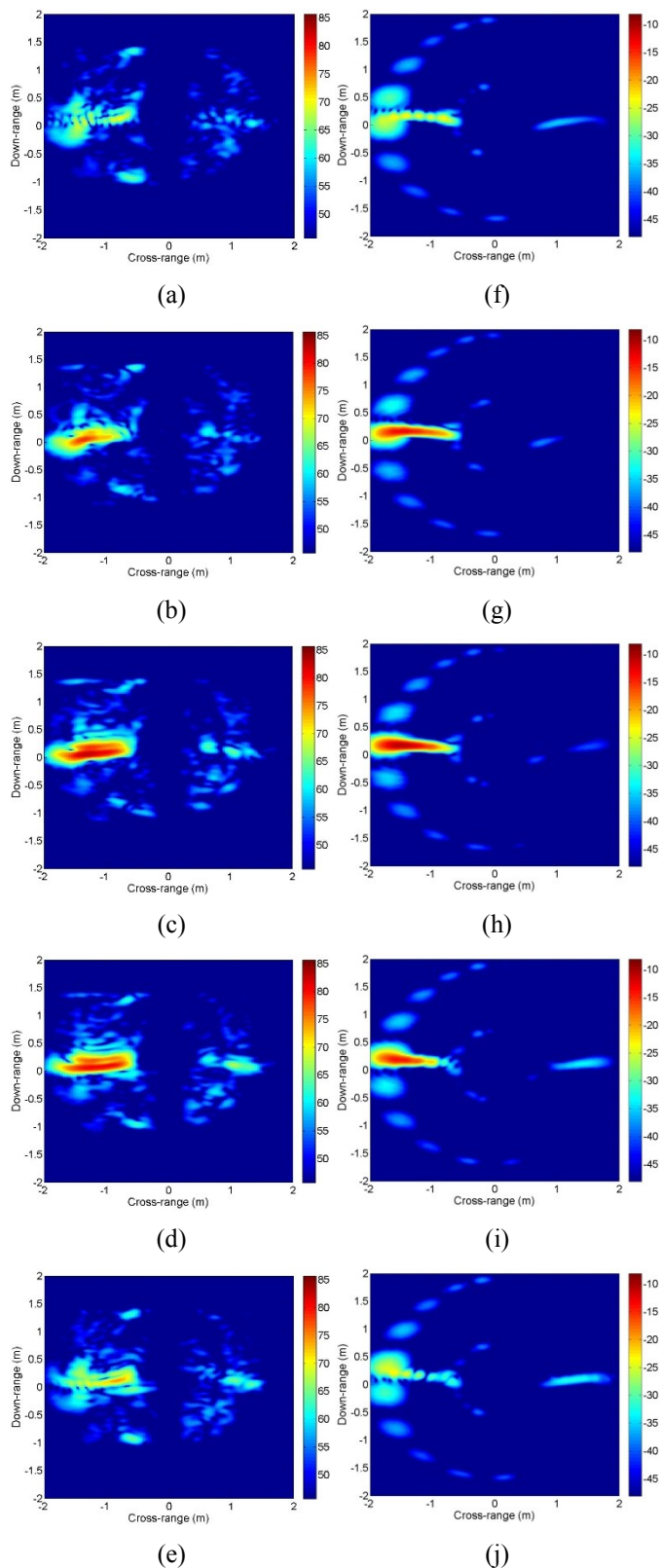

Fig. 5. ISAR snapshots. (a)-(e) Measurement. (f)-(j) Simulation.

D. Composite Image

While the ISAR images already reveal the key target features, it is also possible to obtain a 'complete image' of the windmill. To do so, we rotate each ISAR snapshot by the appropriate angle and incoherently fuse the images into one. Thus, each blade will flash at its respective location on the windmill. This becomes analogous to the wide-angle SAR imaging scenario. In this case, we use 18 non-overlapping angular swaths to generate the image. Furthermore, to better highlight the turbine, a 25 dB threshold was used. Fig. 6 shows the resulting composite image from both measurement and simulation. We can see, in both Fig. 6(a) and 6(b), an image that distinctly captures the outlines of all 18 blades of the windmill. A faint outline of the center ring can be seen in-between the blade flashes in measurement data.
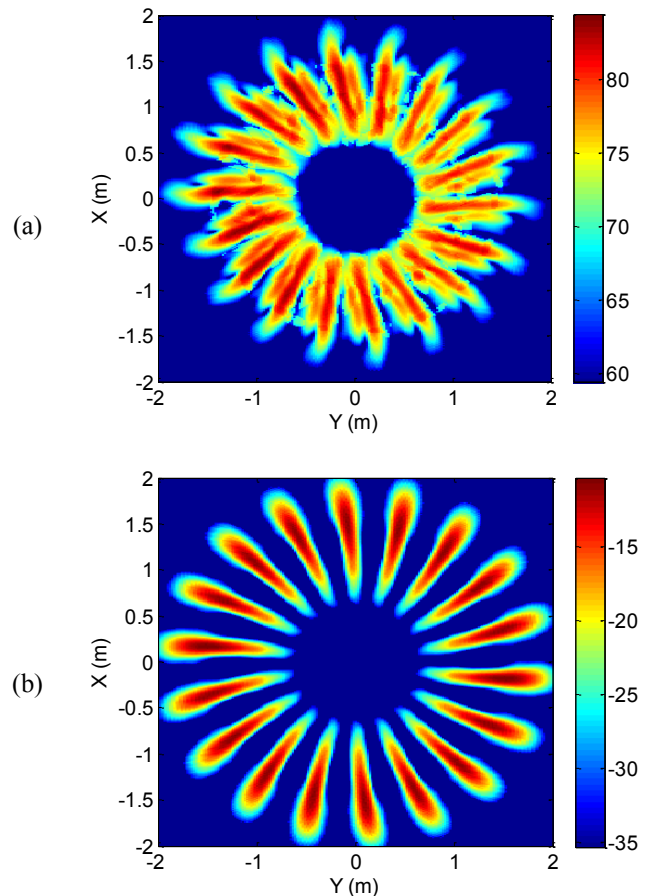

Fig. 6. Windmill composite image. (a) Measurement. (b) Simulation.

IV. DISCUSSIONS

In this section, we discuss some of the subtleties in the image formation process. First, note that the windmill was fully imaged in Fig. 6(a) despite not having its full down-range extent being captured in measurement, as discussed earlier in Fig. 3(a). From Fig. 5(c), it is clear that the windmill return is dominated by the blade flash near zero down-range. Since each blade was fully captured in Doppler (or cross-range), the

windmill can be successfully reconstructed in the composite image after capturing all 18 blade flashes.

Second, we applied the small-angle, narrow-band approximation shown in eq. (3) in the image formation. To test the appropriateness of this approximation over the 20° imaging swath, we have also implemented a polar-reformatting operation before the 2-D IFFT step and tested it on simulation data. The difference in the image quality was minor.

Third, the far-field distance of the windmill using the standard $2(size)^2/\lambda$ formula gives a value which is larger than the 25 m distance in the measurement. However, it was found through simulation that the images generated from 25 m near-field data are not significantly different from those based on far-field data. Should near-field effect become important, it may require the application of a near-field-to-far-field transformation [14].

Finally, higher order motions such as yaw angle and rotation rate changes were not considered in the measurement post-processing. In our data, the effects of higher order motions on the final image were not noticeable. In more severe cases, such as significant deceleration of the windmill, the resulting composite image will be distorted. In such cases, additional motion compensation techniques should be considered [13].

V. CONCLUSION

In this paper, we have presented measured and simulated radar images of an 18-blade windmill. Radar imagery provides revealing information on the scattering phenomenology that is unique to the blade shape. The resulting images may be used in such applications as radar cross-section reduction and structural health monitoring. For example, an image can reveal spatial information on portions of the blade that give rise to the strongest scattering, which could be useful in the design of stealthy turbine blades [15, 16]. Similarly, radar imaging may potentially be used for monitoring the motion anomalies of the turbine blades for structural health monitoring. Work is under way to extend the measurement and simulation to large, utility class wind turbines.

REFERENCES

[1] The Effects of Wind Turbine Farms on Air Defence Radars, Air Warfare Center, Royal Air Force, UK, Jan. 2005.

[2] Report to the Congressional Defense Committees on The Effect of Windmill Farms On Military Readiness, United States Department of Defense Report to the Congressional Defense Committees, Aug. 2006.

[3] Radar, Radio Links, and Wind Turbines, 60th IEA Topical Expert Meeting, Senternovem, Netherlands, Nov. 18-19, 2009.

[4] H. Ling, M. F. Hamilton, R. Bhalla, W. E. Brown, T. A. Hay, N. J. Whitelonis, S.-T. Yang and A. Naqvi, "Assessment of offshore wind farm effects on sea surface, subsurface and airborne electronic systems," Final Report for DE-EE0005380, Dept. of Energy, Sept. 2013.

[5] B. M. Kent, A. Buterbaugh, K.C. Hill, G. Zelinksi, R. Hawley, L. Cravens, T. Van, C. Vogel, and T. Coveyou, "Dynamic radar cross section and radar Doppler measurements of commercial General

Electric windmill power turbines part 1 – predicted and measured radar signatures," *IEEE Antennas Propag. Mag.*, vol. 50, no. 2, pp. 211-219, Apr. 2008.

[6] G. Greving, W.-D. Biermann, and R. Mundt, "On the relevance of the measured or calculated RCS for objects on the ground – case wind turbines," in *Proc. European Conf. Antennas Propag. (EuCAP),* Berlin, Germany, pp. 2216-2220, Mar. 2009.

[7] E. Van Lil, D. Trappeniers, J. De Belser, and A. Van de Capelle, "Computations of radar returns of wind turbines," in *Proc. European Conf. Antennas Propag. (EuCAP)*, Berlin, Germany, pp. 3852-3856, Mar. 2009.

[8] I. Angulo, D. de la Vega, O. Rodriguez, O. Grande, and D. Guerra, "Analysis of the mast contribution to the scattering pattern of wind turbines in the UHF band," in *Proc. European Conf. Antennas Propag. (EuCAP)*, Rome, Italy, pp. 707-711, Apr. 2011.

[9] A. Naqvi, S.-T. Yang, and H. Ling, "Investigation of Doppler features from wind turbine scattering," *IEEE Antennas Wireless Propag. Lett.*, vol. 9, pp. 485-488, 2010.

[10] A. Belmonte and X. Fabregas, "Analysis of wind turbines blockage on Doppler weather radar beams," *IEEE Antennas Wireless Propag. Lett.*, vol 9, pp. 670–673, 2010.

[11] PulsON 410, Time Domain, Huntsville, AL, 2013 [Online]. Available: http://www.timedomain.com/p400-mrm.php

[12] FEKO Version 6.2, EM Software & Systems-S.A., Stellenbosch, South Africa, 2012 [Online]. Available: http://www.feko.info

[13] M. Soumekh, *Synthetic Aperture Radar Signal Processing with MATLAB Algorithms*, New York: Wiley, 1999.

[14] N. Whitelonis, S.-T. Yang and H. Ling, "Application of near-field to far-field transformation to Doppler features from wind turbine scattering," *IEEE Trans. Antennas Propagat.*, vol. 60, pp. 1660-1665, March 2012.

[15] J. Pinto, J. C. G. Matthews, and C. Sarno, "Stealth technology for wind turbines," *IET Radar Sonar Navig.*, vol. 4, pp. 126–133, 2010.

[16] J. J. McDonald, B. C. Brock, S. E. Allen, P. G. Clem, J. A. Paquette, W. E. Patitz, W. K. Miller, D. A. Calkins, and H. J. Loui, "Radar-cross-section reduction of wind turbines (Part 1)," Sandia National Labs, Rept. SAND2012-0480, Mar. 2012.